Astronomy & Astrophysics manuscript no. bootes
May 21, 2009

Deep Low-Frequency Radio Observations of the NOAO Boötes Field

I. Data Reduction and Catalog Construction

H.T. Intema[1], R.J. van Weeren[1], D.V. Lal[2,3], and H.J.A. Röttgering[1]

[1] Leiden Observatory, Leiden University, P.O.Box 9513, NL-2300 RA, Leiden, The Netherlands
[2] National Centre for Radio Astrophysics, Univerity of Pune, India
[3] Max-Planck-Institut für Radioastronomie, Bonn, Germany

Received ... / Accepted ...

Abstract

In this paper we present deep, high resolution 150 MHz radio interferometric observations to complement the extensively studied NOAO Boötes field. We provide a description of the observations, data reduction and source catalog construction. From our single pointing GMRT observation of $\sim$ 12 hours we obtain a high resolution ($26'' \times 22''$) image of $\sim$ 11.3 square degrees, fully covering the Boötes field region and beyond, with a central noise level below 0.7 mJy beam^{-1} which rises to 1.5–2 mJy beam^{-1} at the field edge. The catalog of $\sim$ 600 extracted sources is estimated to be $>$ 95 percent complete at the 20 mJy level, while the estimated contamination is $<$ 1 percent. The low RMS position error of $1.24''$ facilitates accurate matching against catalogs at optical, infrared and other wavelengths. The differential source counts, accurately measured down to $\sim$ 20 mJy, are highly consistent with scaled-down source counts at 325 MHz, which indicates a dominant population of FRi and FRii sources. Combination with available deep 1.4 GHz observations yields an accurate determination of spectral indices for $>$ 400 sources down to the lowest 150 MHz flux levels, of which 16 have ultra-steep spectra with spectral indices below -1.3. The detection fraction of the radio sources in K-band is found to drop with radio spectral index, which is in agreement with the known correlation between spectral index and redshift.

Key words. Surveys – Galaxies:active – Radio continuum: galaxies

1. Introduction

Surveying the radio sky at low frequencies ($\lesssim$ 300 MHz) is a unique tool to investigate many questions related to the formation and evolution of massive galaxies, quasars and clusters of galaxies. Unlike optical light, cosmic radio waves suffer little from cosmic extinction. Combined with the fact that radio sources are often bright, and large as compared to optically visible galaxy content, makes radio sources optimal targets for cosmological studies. Low frequency radio observations benefit from the steepness of radio spectra of various types of cosmic radio sources, like distant radio galaxies and diffuse halo & relic emission from galaxy clusters. The low frequency domain is relatively unexplored due to the relatively low angular resolution and due to the limited sensitivity caused by man-made radio frequency interference (RFI), ionospheric phase distortions and wide-field imaging problems. Recent developments make it possible to survey the low frequency sky at high resolution and high dynamic range.

Luminous, high-redshift ($z > 2$) radio galaxies (HzRGs) are amongst the most massive galaxies in the early Universe (e.g., Röttgering 2006; Seymour et al. 2007; Miley & De Breuck 2008). They generally possess clumpy optical morphologies (Miley et al. 2006), have a large reservoir of dust and ionised and molecular gas (e.g., Reuland et al. 2007), and undergo prodigious star formation, of up to several thousand solar masses per year (e.g., Dey et al. 1997). High redshift radio galaxies are usually located in forming galaxy clusters with total masses of more than 10^{14} M$_\odot$ (e.g., Venemans et al. 2007). Deep optical and infrared studies indicate that we are witnessing the formation of the cluster red sequence (Zirm et al. 2008). Taking into account the short radio lifetimes (few times 10^7 yr), the statistics are consistent with every dominant cluster galaxy having gone through a luminous radio phase during its evolution.

The most efficient way of finding distant luminous radio galaxies is to focus on radio sources having ultra-steep spectra (USS; Röttgering et al 1997; De Breuck et al. 2002). This was recently reinforced by Klamer et al. (2006) who showed that the radio spectra of distant radio galaxies in general do not show spectral curvature, but are straight. Concentrating on the faintest sources from surveys made at the lowest frequencies is therefore an obvious way of pushing the distance limit for radio galaxies beyond the present highest redshift of TN J0924-2201 at $z = 5.1$ (Van Breugel et al. 1999) and probing massive galaxy formation into the epoch of reionization.

The Boötes field is the only large northern field that has been targeted by surveys spanning the entire electromagnetic spectrum. This field has been extensively surveyed

---

Send offprint requests to: H.T. Intema,
e-mail: `intema@strw.leidenuniv.nl`

with radio telescopes including the WSRT[1] at 1.4 GHz (De Vries et al.2002) and the VLA[2] at 74 and 325 MHz (Intema et al. *in preparation*; Croft et al. 2008). The large northern NOAO Deep Wide Field Survey (NDWFS; Jannuzi & Dey 1999) provided 6 colour images ($B_W\,R\,I\,J\,H\,K$) to very faint optical and nearinfrared (NIR) flux limits. Deeper NIR images in $J\,K_S$ are available from the FLAMINGOS Extragalactic Survey (FLAMEX; Elston et al. 2006), while additional z-band images are available from the zBootes campaign (Cool 2007). The entire area has also been surveyed by Spitzer in seven IR bands ranging from 3.6 to 160 μm (Eisenhardt et al. 2004; Houck et al. 2005). Chandra has covered this area in the energy range of 0.5–7 keV to a depth of $\sim 10^{-14}$ ergs s^{-1} cm^{-2}, yielding 3200 quasars and 30 luminous X-ray clusters up to redshift $z \sim 1$ (Murray et al. 2005; Kenter et al. 2005). The UV space telescope GALEX has covered the Boötes field. All the 10,000 galaxies brighter than $R < 19.2$ and X-ray / IRAC / MIPS QSOs brighter than $R < 21.5$ have redshifts through the AGES project (Kochanek et al. *in preparation*).

Given the size of the GMRT field-of-view (FoV; $\sim$ 3.5 degrees) and angular resolution ($\sim 25''$) at 150 MHz, the Boötes field is a well-matched region for conducting a deep survey. Combined with the existing multi-wavelength surveys, our deep 150 MHz Boötes field observations will allow for the first time a complete population study of faint ($\gtrsim$ 10 mJy) low frequency radio sources. The characteristics of the survey are such that at $L_\star$ elliptical galaxies and radio sources with a radio luminosity comparable to the FRI/FRII break ($L_{1.5} \approx 3 \times 10^{24}$ W Hz^{-1} sr^{-1}) are detectable at $z \sim 2$. Based on models from Jarvis et al. (2001), we predict that there are 5–10 objects of the very steep spectrum variety, that are possible contenders for very high ($z > 5$) redshift galaxies (Figure 1). Based on the shallow Spitzer data, already 3 radio galaxies with photometric redshifts of $z > 4$ have been identified in the Boötes field (Croft et al. 2008). Also, Cool et al. (2006) report the discovery of 3 quasars with spectroscopic redshifts $z > 5$, while McGreer et al. (2006) found a quasar at $z = 6.1$.

Deep observations at low frequencies are typically limited by the difficulty of handling the corrupting influence of the ionosphere on the visibility data. For the data reduction, we make use of the recently developed SPAM calibration software that solves for spatially variant phase errors (Intema et al. 2009 & *in preparation*). This has yielded significant improvements in the dynamic range and image reliability of several VLA 74 MHz fields as compared to previously existing calibration methods.

In Section 2 we describe the GMRT 150 MHz observations and data reduction. In Section 3, we present details on the source extraction and catalog construction. Section 4 contains an initial analysis of the source population. A discussion and conclusions are presented in Section 5. Throughout the article, source positions are given in epoch J2000 coordinates.

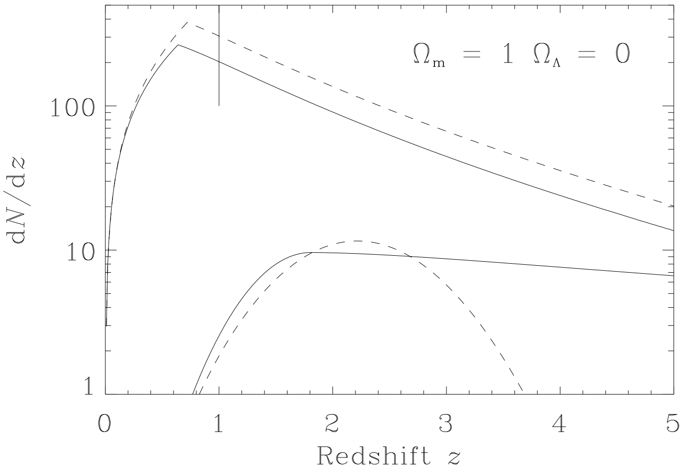

Figure 1: Model redshift distributions for a 3 mJy survey at 150 MHz, assuming a mean spectral index $\alpha = -0.8$. They were calculated using the radio luminosity functions of Willott et al. (2000), using 3CRR, 6C and 7C complete redshift surveys at 151 MHz which comprises 357 sources. The solid lines represent the z-distribution if there is no redshift cut-off (constant space density beyond the peak at $z = 2.5$) and the dashed lines for a radio luminosity function with a redshift cut-off (at about $z = 2.5$) modelled by a Gaussian. The upper curves are for the low-luminosity AGN population which includes FRIs and low-excitation / weak emission line FRIIs. The redshift distribution for these is *completely unconstrained* with our data beyond $z \sim 1$, denoted by the solid vertical line, so its just an extrapolation. The lower curves are for the powerful FRII-s. These are well constrained up to $z = 3$.

2. Observations and Data Reduction

In this Section, we describe the observing instrument, strategy and the data reduction steps that led to the production of the 150 MHz survey area image. Data reduction of low frequency radio observations differs most noticeably from traditional higher frequency observations by the wide FoV that needs to be imaged and deconvolved, and the spatial variability of ionospheric phase errors across the FoV of individual antennas. These issues and our solution methods are addressed in the following text.

2.1. Observations

The Indian Giant Metrewave Radio Telescope (GMRT; e.g., Nityananda 2003) is an interferometer consisting of 30 antennas, with nearly half the antennas located at random positions in a central square kilometer, and the remaining antennas distributed in an approximate Y-shape. The non-coplanar configuration provides baseline lengths from $\sim$ 50 m up to 30 km, covering almost three orders of magnitude in spatial scales on the sky. The 45 meter dish diameter makes the GMRT suitable for efficient observing down to the lowest frequency (currently 150 MHz). The field-of-view (FoV) diameter at 150 MHz, defined by the half-power beam width (HPBW), is 3.1 degrees, while the resolution is typically 20–25$''$. At 150 MHz, the effectiveness of the the shortest baselines (mostly withing the central square) is compromised due to the presence of strong RFI within the full observing bandwidth. Also, the low observing frequency, in combination with the low latitude location of GMRT relatively near the geomagnetic equator, results in

---

[1] Westerbork Synthesis Radio Telescope

[2] Very Large Array

Date	June 3, 2005	June 4, 2005
LST range	12–20 hours	10–19 hours
local time[a] range	20:00–04:00	18:00–03:00
Time on target	359 min	397 min
Primary calibrator	3C 286	3C 286
Time on calibrator	94 min	108 min

[a] Indian Standard Time (IST) = Universal Time (UT) + 5:30

Table 1: Overview of GMRT observations on the Boötes field.

an increase of ionospheric phase rotations that vary with time and viewing direction.

The Boötes field was observed with the GMRT during two consecutive nights (Table 1), with the pointing center at $14^{\mathrm{h}}32^{\mathrm{m}}05.75^{\mathrm{s}}$ right ascension and $+34°16'47.5''$ declination. Visibilities were recorded each 16.8 seconds in a single sideband of 8.0 MHz centered at 153.1 MHz, comprising 128 channels of 62.5 KHz each, in two circular polarizations (RR and LL). The bandwidth was narrowed to 6 MHz by an additional antenna-based bandpass filter to reduce the effect of man-made radio frequency interference (RFI) at the edges of the observing band. Observing in the spectral channel mode allows for excision of narrow-band RFI in the observing band, and for reducing bandwidth smearing during imaging.

During both nights, the target field was observed in time blocks of 36 minutes, alternated with 8 minute observations on the calibrator (3C 286). The relatively high overhead in calibrator observations was justified by the need to monitor the GMRT system stability, RFI conditions and ionospheric conditions, and to optimize consistency of the flux scale over time. The directional variation of ionospheric phase errors between calibrator and target field compromises the astrometric accuracy when transferring the calibrator phase solutions. There were typically 27 antennas available during each observing run. A $\sim$ 2 hour power failure at the start of the first observation night caused a $\sim$ 1 hour effective loss of observing time.

2.2. Data Reduction

The total data reduction was performed in two stages. The first stage consisted of a ‘traditional’ calibration approach, in which the flux scale, bandpass shapes and phase offsets are determined from the calibrator observations, transferred to the target field data, after which the target field was self-calibrated and imaged for several rounds (details follow below). Despite the good overall quality of the self-calibrated image from the first stage, there were significant artefacts present in the background near the bright sources, limiting the local dynamic range to a few hundred. Direction-dependent ionospheric phase errors are a main cause of these artefacts. Therefore, during the second stage of the data reduction, we made use of the (recent) SPAM software package (Intema et al. 2009) that incorporates direction-dependent ionospheric phase calibration. SPAM measures the antenna-based, direction-dependent phase errors by peeling bright sources in the FoV (Noordam 2004, separates (constant) instrumental and (time- and spatially variable) ionospheric phase contributions, combines the ionospheric phases into a consistent phase screem model, and predicts the ionospheric phase corrections in arbitrary viewing directions while imaging the FoV.

2.2.1. Traditional Calibration

For calibration against 3C 286, we adopted a point source model with a flux of 31.01 Jy from the Perley-Taylor 1999.2 scale[3]. The following reduction steps are performed independently on the data sets from both nights.

For the first phase of data reduction, we used the Astronomical Image Processing Sofware (AIPS; e.g. Bridle & Greisen 1994) package, developed by the National Radio Astronomy Observatory (NRAO). A first round of flagging consisted of removal of dead and malfunctioning antennas and baselines, systematic removal of the first 30 seconds of each observing time blocks due to potential system instabilities, and manual and semi-automated flagging of channels and time ranges on individual baselines, based on excessive ($\gtrsim$ 5 times the RMS) visibility amplitudes. An initial phase calibration was performed on 3C 286 on the highest possible (16.8 sec) time resolution, using a small, (relatively) RFI-free channel range. Bandpass calibration on 3C 286 (normalized to the same channel range) was followed by a combined amplitude and phase (A&P) calibration on the same source on a 10 minute time scale. The bandpass, amplitude and (combined) phase calibration was transferred to the target field data. The outer channels of the target field data were dropped due to excessive noise and RFI (17 channels in total).

The target field data of the first night was imaged (see Table 2), followed by three rounds of phase-only self-calibration & imaging (60, 30 and 16.8 seconds time resolution, respectively) and one final round of (60 seconds) A&P self-calibration & imaging using gain normalization to preserve the flux scale. The data from both nights were A&P calibrated (normalized, 16.8 sec) against this target field model, after which the target field model was subtracted from the visibilities. The residuals were manually and semi-automatically flagged per baseline for excessive visibility amplitudes, after which the model was added back. The resulting visibility data sets for both nights were combined into one data set, followed by imaging. The (gaussian fitted) RMS of the image background, measured over the inner half of the (uncorrected) primary beam area, is approximately 1.4 mJy beam^{-1}. Near the brightest three sources with apparent fluxes larger than 1 Jy, the background RMS locally rises above 2.2 mJy beam^{-1}.

2.2.2. Direction-dependent Phase Calibration

In general, the time variations in the antenna-based phase corrections from self-calibration indicated that the ionospheric conditions were relatively quiet. This was further strengthened by a visual inspection of the 150 MHz image, which showed many fairly undistorted, compact point sources that match well with source positions from the 1.4 GHz NVSS catalog (Condon et al. 1994, 1998). But, as stated earlier, the presence of significant image artefacts

---

[3] Defined in the ‘VLA Calibrator Manual’, available online through *http://www.vla.nrao.edu/astro/calib/manual/baars.html*

Field diameter	$6.8°^a$
Pixel size	$4''$
Weighting	robust 0.5^b
Wide-field imaging	polyhedron (facet-based)[c]
Number of initial facets	199
Facet diameter	0.57°
Facet separation	0.47°
Deconvolution	Cotton-Schwab CLEAN[d]
CLEAN box threshold	$5\,\sigma$
CLEAN depth	$2\,\sigma$
Restoring beam	$26'' \times 22''$ (78°)

[a] We map more than twice the HPBW diameter to allow for deconvolution of nearby bright sources.
[b] Briggs 1995
[c] Perley 1989; Cornwell & Perley 1992
[d] Schwab 1984; Cotton 1999; Cornwell, Braun & Briggs 1999

Table 2: Overview of the wide-field imaging parameters.

Calibration cycles	2
Peeled sources[a]	24
Number of added facets	24
Layer heights (weights)	100 km (0.25) 200 km (0.50) 400 km (0.25)
Parameter γ^b	5 / 3
Model parameters	20
Model fit phase RMS[a]	$19.2° \pm 3.0°$
Peeling corrections applied	yes
Reference catalog	NVSS[c]

[a] Specified for the final (second) calibration cycle only.
[b] Power-law slope of the assumed phase structure function.
[c] Condon et al. 1994, 1998

Table 3: Overview of the SPAM processing parameters. For more information on the meaning of the parameters we refer to Intema et al. (2009 & *in preparation*).

near the brightest sources indicated that the image quality could be further improved by including direction-dependent phase corrections through SPAM. This package uses the ParselTongue interface (Kettenis et al. 2006) to access AIPS tasks and files from the Python programming environment, while providing a collection of high-level tasks for basic calibration and imaging and for calibration of direction-dependent ionospheric phase errors.

For our data sets, we noticed discontinuous phase behaviour in the calibration solutions on several antennas that was clearly of instrumental origin. SPAM is able to correct for slow instrumental phase drifts on a few antennas (Intema et al. *in preparation*), but not for abrupt transitions. Self-calibration is relatively unconstrained and can solve for antenna-based phase discontinuities, but lacks directional variability. Applying both self-calibration and SPAM seems a logical option, although the combined effect is difficult to predict because self-calibration invalidates the SPAM assumption of constant instrumental phases. Under quiet ionospheric conditions, when the phase structure over the array for different viewing directions is dominated by slowly varying gradients, self-calibration may approximately solve for an overall phase gradient but not for any higher order phase structure. Applying SPAM after self-calibration can be considered as a perturbation to the overall gradient correction.

For the data reduction presented here, complementing self-calibration with SPAM resulted in a significant reduction of background noise, most noticeable near the bright sources. The self-calibrated data set (collapsed into 27 frequency channels & polarizations combined into stokes I) and source model are used as an initial estimate to start the SPAM calibration cycle, consisting of the following steps:

1. Subtract the target field source model from the visibility data while applying the (direction-dependent) phase calibration corrections. Peel apparently bright sources.
2. Fit an ionospheric phase model to the peeling solutions.
3. Apply the ionospheric phase model phases during re-imaging of the target field.

For the first cycle, there are no phase corrections available yet for step 1, therefore omitted. The total SPAM calibration consisted of two cycles, for which relevant parameters are given in Table 3. We used the same imaging parameters as given in Table 2, but centered an additional 24 facets at the locations of the peeled sources to minimize pixellation effects (e.g., Cotton & Uson 2008)). The image background RMS in the inner half of the primary beam area is approximately 1.0 mJy beam^{-1}, while the local noise near the apparent brightest three sources remains below 1.45 mJy beam^{-1}. Because all three bright sources are at or beyond the HPBW, we expect that the remaining background artefacts are dominated by visibility amplitude errors due to residual RFI, pointing errors and rotating, non-circular primary beam patterns (e.g., Bhatnagar 2008).

3. Catalog Construction

In this Section we describe details on the construction of the source catalog that was extracted from the 150 MHz image of the Boötes field. The resulting image after SPAM calibration was scaled down by 4 percent to incorporate a correction to the flux calibrator scale (see Section 3.4). Next, the was corrected for primary beam attenuation with a circular beam model[4]

$$\begin{aligned} A(\theta,\nu) \;=\; & 1 - 4.04\,10^{-3}(\theta\nu)^2 + 76.2\,10^{-7}(\theta\nu)^4 \\ & -68.8\,10^{-3}(\theta\nu)^6 + 22.03\,10^{-3}(\theta\nu)^8, \end{aligned} \tag{1}$$

where θ is the angular distance from the pointing center in arcminutes and ν the observing frequency in GHz. As the fractional bandwidth is small ($<$ 4percent), we use same the central frequency (153.1 MHz) beam model for all frequency channels. The image area is limited to $A(\theta,\nu) > 0.3$ to limit the propagation of inaccuracies in the primary beam model and to limit the increase of background noise near the edge, which yields a circular survey area of 11.3 square degrees. Figure 2 shows a map of the local background RMS of the

---

[4] From the GMRT User Manual

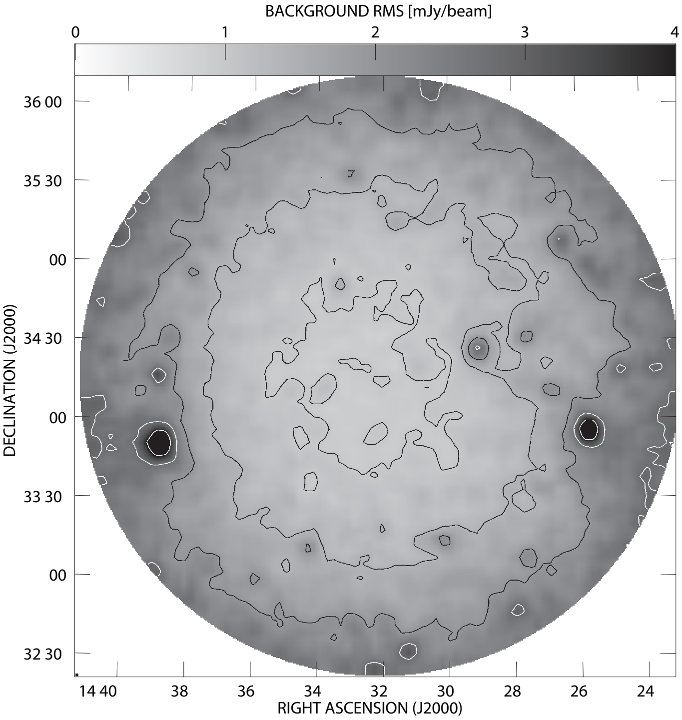

Figure 2: The grayscale map represents the local background RMS as measured in the Boötes field image. The overplotted contours mark lines of equal RMS at $[0.7, 1.0, 1.4]$ mJy beam^{-1} (black) and $[2.0, 2.8, 4.0]$ mJy beam^{-1} (white). The local enhancements in RMS coincide with the positions of the brightest sources.

circular survey area, which has a large central area with a background RMS below 1.0 mJy beam^{-1}, a global increase of the local noise to 1.5–2 mJy beam^{-1} when moving towards the field edge, and several small areas around bright sources where the local noise is roughly twice the surrounding noise level. The overall background RMS is found to be 1.7 mJy beam^{-1}.

For an observation of $\sim$ 10 hours, the theoretical thermal noise level for GMRT at 150 MHz is estimated to be $\sim 0.2 - 0.3$ mJy beam^{-1}[5]. For our observation, the measured noise level in the center part of the field is a factor of 2–4 higher. We think this is mainly the combined result of residual RFI and residual calibration errors. For the latter category, we expect that pointing errors and non-circular symmetry in the primary beam patterns are the main cause for residual sidelobe noise, most apparent around the bright sources (e.g., Bhatnagar 2008).

Although we used multi-frequency synthesis during imaging, the 0.25 MHz width of individual frequency channels causes bandwidth smearing during imaging. Applying the standard formula (e.g., Thompson 1999) to our case, the radial widening of sources at the edge of the field (at 1.9 degree from the pointing center) is estimated to be $\sim 11''$, which is half the minor axis of the restoring beam. Similarly, the visibility time resolution of 16.8 sec causes time averaging smearing in the order of $\sim 8''$ at the field's edge. This may appear problematic, but the majority of sources are detected within the inner part of the primary beam (both effects scale linearly with radial distance from the pointing center), and the total flux of smeared sources is conserved.

3.1. Source Extraction

We used the *Blob Detection & Source Measurement* (BDSM) software package[6] to extract sources from our image. With our settings, BDSM estimates the local background noise level σ_{L} over the map area, searches for peaks $> 5\,\sigma_{\mathrm{L}}$, expands the $5\,\sigma_{\mathrm{L}}$ detections into islands by searching for adjacent pixels $> 3\,\sigma_{\mathrm{L}}$ (rejecting islands smaller than 4 pixels), fits the emission in the islands with gaussians, and estimates the fluxes, shapes and positions of sources (including error estimates) both by grouping of fitted gaussians into sources and by a direct moments analysis of the island pixels. Uncertainties in the source flux, position and shape measurements are estimated following Condon 1997. For more details, we refer to the BDSM manual[7].

BDSM detected 644 islands, for which the 935 fitted gaussians were grouped into 696 distinct sources. Of these, 499 sources were fitted with a single gaussian. Visual inspection of the image, complemented with a comparison against a very deep 1.4 GHz map (see Section 3.3), resulted in the removal of 16 source detections in the near vicinity of six of the seven brightest sources. We also removed 4 sources that extended beyond the edge of the image. To facilitate total flux measurements at the high flux end, we combined multiple source detections in single islands, and manually combined 50 additional source detections that were assigned to different islands but appeared to be associated in either the 150 MHz image or the deep 1.4 GHz map. The combined flux is the sum of the individual components, while the combined position is a flux-weighted average. Error estimates of the positions and fluxes of the components are propagated into error estimates of the combined flux and position. The final catalog consists of 598 sources.

3.2. Completeness and Contamination

We estimate the completeness of the 150 MHz catalog by performing Monte-Carlo simulations. The source extraction process generated a residual image from which all detected source flux was subtracted. For our simulation, we inserted 1000 fake point sources into the residual image, and used the same mechanism as described in Section 3.1 to extract them. The fake source positions were selected randomly, but never within $50''$ of another source, a blanked region (near the image edge) or a > 10 mJy residual. The source fluxes S were chosen randomly within the range 3 mJy to 3 Jy, while obeying the source count statistic $dN/dS \propto S^{-1.5}$, which produced statistically sufficient detection counts in all logarithmic flux bins (except in the highest flux bins) The simulation was repeated 20 times to improve the accuracy and to derive error estimates. The detection fractions are plotted in Figure 3. From this plot, the estimated completeness is $\sim$ 70 percent at 10 mJy and $\sim$ 99 percent at 20 mJy.

In this approach we have ignored several effects that may influence the detectability of sources, like (i) the in-

---

[5] From the GMRT User Manual

[6] version 2.1, available through *http://www.strw.leidenuniv.nl/~mohan/anaamika*

[7] *http://www.strw.leidenuniv.nl/~mohan/anaamika_manual.pdf*

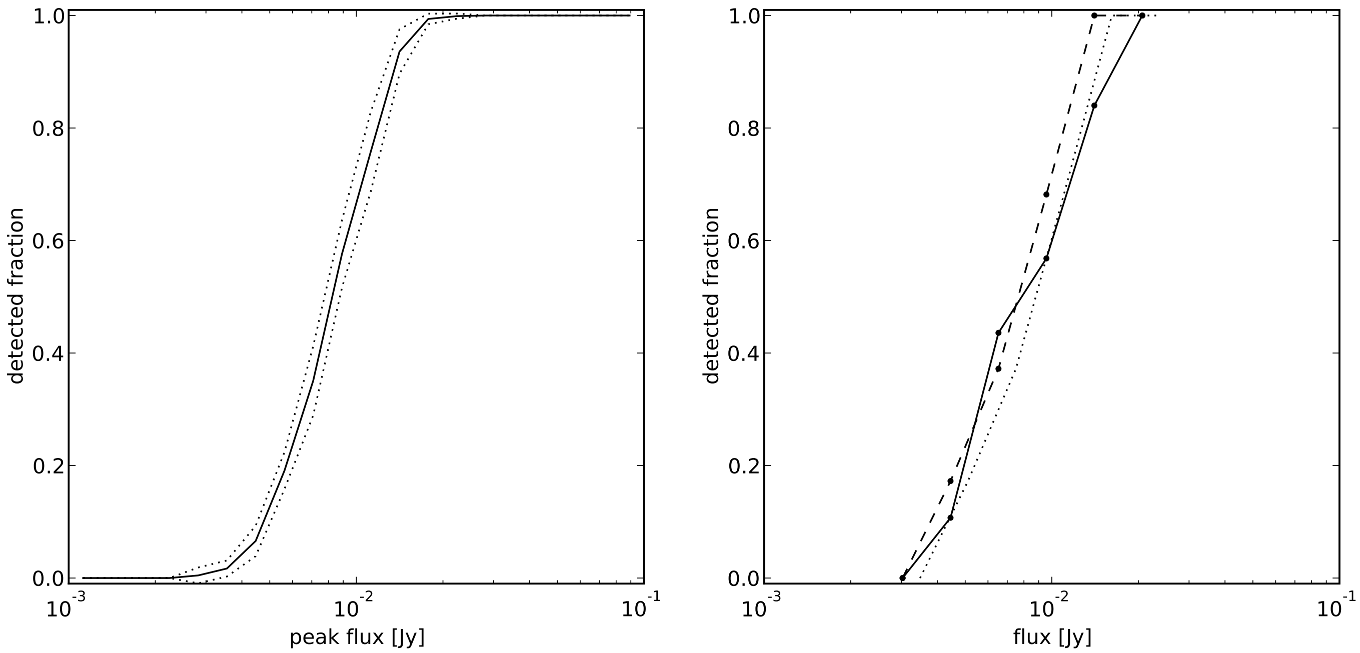

Figure 3: Detection fractions as a function of flux. *Left*: Result from 20 Monte-Carlo simulations, in which 1000 point sources with varying fluxes were inserted into the residual image, followed by a source extraction. The horizontal axis denotes the input (peak) flux. The solid line is the average detection fraction, and the dotted lines denote the $1\,\sigma$ uncertainty. *Right*: Result from scaling the peak flux and total flux of a subset of high S/N sources with varying sizes down to the detection limit, and applying the $5\,\sigma_{\mathrm{L}}$ detection criteria. The dashed line is the detection fraction as a function of peak flux, the solid line is the detection fraction as a function of total flux, and the dotted line is the dashed line shifted in flux by 15 percent to approximately match the solid line.

trinsic size of sources, (ii) calibration errors, and (iii) imaging and deconvolution. The source detection algorithm uses a peak detection threshold, therefore sources that are resolved or are defocussed due to calibration errors have a decreased probability of detection. We have no model for the angular size distribution of sources at this frequency, but other observations show that the major fraction of low frequency sources are unresolved at $\sim 25''$ resolution (e.g., Cohen et al. 2004; George & Ishwara-Chandra 2009). From our catalog we find that more than 90 percent of the sources appear to have a simple, near-gaussian morphology. Assuming the angular size distribution of sources changes slowly with source flux, and assuming that calibration and imaging smearing affects all sources in a statistically equal way, we can estimate the resolution bias from the catalog itself. For this purpose, we select a subset of 214 high S/N sources with peak fluxes between $12 - 20\,\sigma_{\mathrm{L}}$ with simple morphology. The flux of these sources was scaled down by a factor of 4 to create a fake population of sources near the detection threshold. After applying the $5\,\sigma_{\mathrm{L}}$ detection criterium, we determined the detection fractions both as a function of peak flux and total (integrated) flux (Figure 3). Although this approach suffers from low number statistics, the general trend of both detection fraction functions is similar but shifted in flux by $\sim$ 15 percent. We therefore continue by assuming that the true completeness is approximated by the point source completeness from the Monte-Carlo simulation, shifted up in flux by 15 percent.

A known effect that arises from the deconvolution process is CLEAN bias (e.g., Condon et al. 1994, 1998; Becker, White & Helfand 1995). This is a systematic negative offset in the recovered fluxes after deconvolution, probably the result of false CLEANing of sidelobe peaks in the dirty beam pattern. One can estimate the CLEAN bias by injecting fake sources into the visibility data and compare the recovered fluxes after imaging & deconvolution with the injected fluxes. We have not attempted this approach, but instead taken precautions to minimize the CLEAN bias effect. In our case, the dirty beam is relatively well-behaved due to a good UV-coverage from two extended observing runs, in combination with multi-frequency synthesis and a robust weighting parameter of 0.5 (slightly towards natural weighting). CLEAN bias is further suppressed through the use of CLEAN boxes in the imaging & deconvolution process.

For an estimate of the contamination of the catalog with fake detections, we compare the the GMRT 150 MHz image and extracted source catalog against the results from a deep WSRT 1.4 GHz survey of the Boötes field by De Vries et al. 2002. The 150 MHz and 1.4 GHz observations are well matched in terms of survey area and resolution ($\sim$ 7 square degrees and $13'' \times 21''$ for WSRT, respectively). The typical background RMS over the WSRT survey area is 28 μJy beam^{-1}. For a spectral index of -0.8, the 1.4 GHz observations are $\sim$ 10 times more sensitive. We restrict our comparison to a 1.4 degree radius circular area to avoid the noisy edge of the deep 1.4 GHz survey. For all of the 399 sources detected at 150 MHz we find a counterpart in the 1.4 GHz map (383 sources were automatically matched within a $25''$ search radius, while the remaining fraction of sources with complex morphology were confirmed manually). We could not match the full GMRT area, but con-

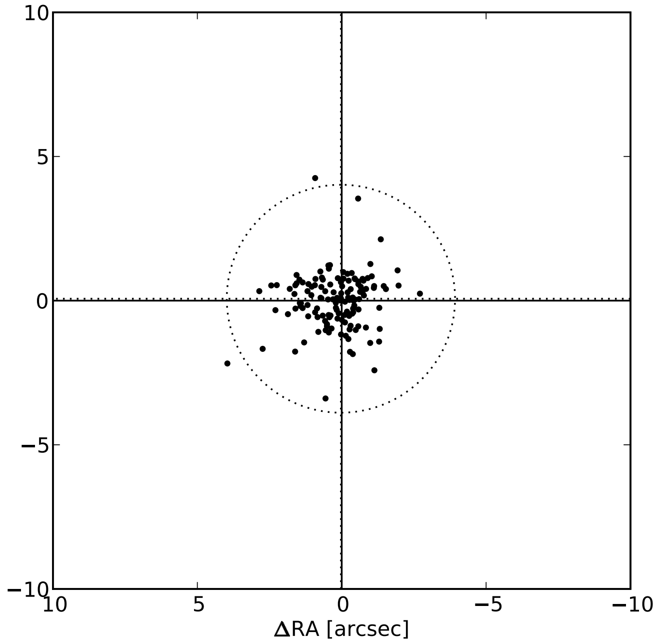

Figure 4: Scatter plot of the position offsets of a bright ($> 10\ \sigma_L$) subset of 126 sources from the GMRT 150 MHz catalog that have a simple (gaussian) flux profile, using the source catalog of the deep 1.4 GHz WSRT observations as the reference. The dotted lines mark the mean position offset, while the dotted circle marks 3 times the RMS scatter around the offset.

sidering that our source extraction is based on local background RMS and that the false detections only occured near a few bright sources, we estimate that the contamination over the full area is < 1 percent.

3.3. Astrometric Accuracy

For an estimate of the astrometric accuracy, we compare the source positions in the GMRT 150 MHz catalog against catalog source positions from the deep WSRT 1.4 GHz map from De Vries et al. For our position comparison, we only use sources whose flux profile is accurately described by a single gaussian, and whose peak flux S is at least $10\,\sigma_{\rm L}$. This bypasses most of the position errors that arise from low signal-to-noise (S/N, or $S/\sigma_{\rm L}$), different grouping of gaussians and spectral variations across sources. Using a search radius of $10''$, we cross-match 126 sources in both catalogs. This number does not change when changing the search radius between $5 - 60''$. These sources appear to be randomly distributed over the selected area.

Figure 4 shows a plot of the position offsets of the 150 MHz sources as compared to their 1.4 GHz counterparts. We measure a small mean position offset in right ascension (RA, or α) and declination (DEC, or δ) of $(\Delta\alpha, \Delta\delta) = (0.11'', 0.09'')$. We correct the catalog positions for this small offset. The estimated RMS scatter around this offset is $\sigma_{\alpha,\delta} = 1.32''$.

Because we are comparing catalogs that both have a limited positional accuracy, the total RMS position scatter is composed of position errors from both. We compared compact sources with high S/N, therefore we may ignore S/N-dependent errors from the fitting process. Under these conditions, the observed scatter can be written as the quadratic sum of the astrometric calibration accuracies of each catalog:

$$(\sigma_{\alpha,\delta})^2 = (\sigma^{1400}_{\alpha,\delta})^2 + (\sigma^{150}_{\alpha,\delta})^2 \qquad (2)$$

The S/N-independent part of the positional accuracy of the 1.4 GHz sources is $0.44''$ (De Vries et al.), therefore we derive an overall astrometric calibration accuracy for the 150 MHz image of $1.24''$. We consider this to be an upper limit, as we did not incorporate the possible position error due to varying spectral indices across sources. We quadratically add this error to the calculated position errors in the 150 MHz source catalog as determined in Section 3.1.

3.4. Flux Scale

The accuracy of the flux scale that is transferred from the calibrator 3C 286 to the target Boötes field is influenced by several factors: (i) the quality of the calibrator observational data, (ii) the accuracy of calibrator source model, and (iii) the difference in observing conditions between the calibrator and target field. Here we discuss issues that influence these factors.

The quality of the calibrator data is most noticeably affected by RFI and by ionospheric phase errors. The repeated observation of 3C 286 every ~ 45 minutes during the observing enabled us to monitor the RFI and ionospheric conditions over time. The mild fluctuations in the initial (short interval) calibration gain phases at the start of the data reduction showed that the ionosphere was very calm during both observing nights, therefore we exclude the possibility of diffraction or focussing effects (e.g., Jacobson & Erickson 1992). Apparent flux loss due to ionospheric phase errors was prevented by applying the (short interval) gain phase corrections before bandpass- and amplitude calibration (see Section 2.2.1).

RFI was continuously present during both observing runs. This roughly consisted of persistent RFI over the full band, most noticeably on the shortest (central square and eighbouring arm antenna) baselines, and of more sporadic events on longer baselines during one or more time stamps and/or narrow frequency ranges. The sporadic events were relatively easy to recognize and excise, but for the persistent RFI this is much harder due to a lack of contrast between healthy and affected data on a single baseline. Some of the shortest, most affected baselines were removed completely. On longer baselines, persistent RFI from quasi-stationary sources can average out due to fringe tracking (Athreya 2009), but does add noise. Large magnitude RFI amplitude errors in the visibilities may result in a suppression of the gain amplitude corrections. Because these effects are hard to quantify, we adopt an ad-hoc 2 percent amplitude error due to RFI.

Because 3C 286 is unresolved ($\lesssim 2.5''$) within a $20 - 25''$ beam, we used a 31.01 Jy point source for the calibrator model (see Section 2.2.1). The utilized Perley-Taylor flux scale is an extrapolatation of VLA flux measurements at 330 MHz and higher, using a fourth order polynomial in log-log space. In Table 4 a comparison is presented between flux measurements of 3C 286 in various sky surveys at low frequencies and the predicted fluxes from the Perley-Taylor model. Although there is a large variation in the flux differences at the different frequencies, there appears to be a

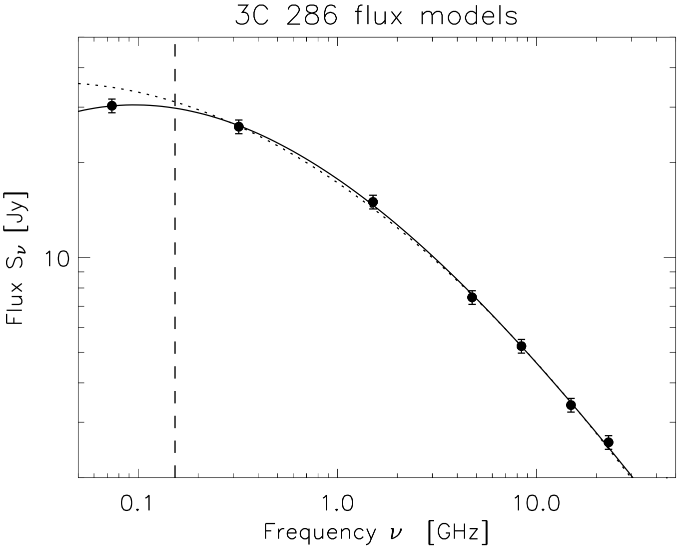

Figure 5: Model of the radio spectrum of 3C 286. The measurements (dots) above 150 MHz (dashed line) were used to fit the original Perley-Taylor 1999.2 model (dotted line), which appears to overestimate the flux at 150 MHz. By adding one measurement at 74 MHz, we fit an alternative model (solid line) that may give a better prediction at 150 MHz.

overestimation by the Perley-Taylor model below 200 MHz. For this reason, we re-fitted the polynomial to the original data points plus the additional 74 MHz VLSS measurement (which we think is most relevant for altering the low frequency behaviour of the model), assuming 5 percent errors for all data points (Figure 5). Our new model is given by:

$$\begin{aligned}\log_{10}(S_\nu) &= 1.24922 - 0.434710\log_{10}(\nu) \\ &\quad -0.174786(\log_{10}(\nu))^2 \\ &\quad +0.0251542(\log_{10}(\nu))^3, \qquad (3)\end{aligned}$$

with ν the frequency in GHz and S_ν the flux in Jy. This model is a slightly better fit to the fluxes from the various surveys (Table 4), although the large scatter remains. For the center of the GMRT band at 153.1 MHz, the new model predicts a flux of 29.77 Jy. We have adopted this new model by scaling the image by the ratio 29.77/31.01 before primary beam correction (Section 3). The accuracy of this flux scale is closely related to the accuracy of the 74 MHz data point, for which a 10 percent flux error is given. Assuming the error in the 330 MHz is much smaller, and 150 MHz is roughly half way from 74 to 330 MHz in logarithmic frequency, we set an upper limit of 5 percent error on the adopted flux scale of 3C 286 at 150 MHz.

A second complication is the presence of other sources in the 3.1 degree FoV around 3C 286, which causes the calibrator model to be incomplete. For example, the total apparent flux in the Boötes field that was extracted through deconvolution is ~ 46 Jy from ~ 1000 sources, which may be typical lower limit for any blind field. If this flux is distributed over many sources that are individually much fainter than the calibrator then the net effect of this additional flux is only noticeable on a small subset of the shortest baselines, while calibration utilizes all baselines. Inspection of the 3C 286 field at 74 MHz (VLSS; Cohen et al. 2007) and 325 MHz (WENSS; Rengelink et al. 1997) does identify two relatively bright sources within 0.7 degrees of 3C 286 with estimated apparent GMRT 150 MHz fluxes of 5.3 and 2.7 Jy, respectively. These sources will cause a modulation of the visibility amplitudes across the UV-plane. We performed a simple simulation, in which we replaced the measured 3C 286 visibilities with noise-less model visibilities of three point sources, being 3C 286 and the two nearby sources, and calibrated these visibilities against a single point source model of 3C 286, using the same settings as in the original data reduction. We found that the combined gain amplitude for all antennas and all time intervals was 1.000 ± 0.004. For individual 10 minute time blocks, the largest deviation from one was 1.00 percent, which indicates the magnitude of the possible error when using a single 10 minute calibrator observation on 3C 286. The small deviations per time block are transferred to the target field data, but these are suppressed by amplitude self-calibration against the target field source model. We set an upper limit of 1 percent due to the presence of other sources in the FoV of the calibrator.

While transferring the flux scale from calibrator to target field, the derived gain amplitudes need to be corrected for differences in sky temperature due to galactic diffuse radio emission (e.g., Tasse et al. 2007), which is detected by individual array antennas but not by the interferometer. The GMRT does not implement a sky temperature measurement, therefore we need to rely on an external source of information. From the Haslam et al. (1982) all-sky map, we find that the mean off-source sky temperatures at 408 MHz as measured in the 3C 286 and Boötes field are both approximately 20 ± 1 degree. Applying the formulae given by Tasse et al. for the GMRT at 150 MHz[8], we estimate a gain inaccuracy of ~ 2 percent at most.

Another effect that may influence the gain amplitude transfer between calibrator and target field is an elevation-dependent gain error. This is a combination of effect like structural deformation of the antenna, atmospheric refraction and changes in system temperature from ground radiation. According to Chandra, Ray & Bhatnagar 2004, the effect on amplitude is rather small, if not negligible, for GMRT frequencies of 610 MHz and below. Furthermore, the relatively short angular distance of 13.4 degrees between 3C 286 and the target field center causes the differential elevation error to be limited. Elevation dependent *phase* errors are not relevant, because we don't rely on the calibrator to restore the astrometry. For our observation, we assume that elevation-dependent effects can be ignored.

To incorporate the effects discussed above plus some margin, we quadratically add a relative flux error of 10 percent to the flux measurement errors in the source catalog.

4. Analysis

The ~ 600 radio sources in our 150 MHz catalog form a statistically significant set, ranging in flux from 3.9 Jy down to 5.1 mJy. Because of the large survey area, cosmic variance is expected to be small. The large variety of available catalogs at other frequencies allows for a nearly endless number of ways to combine information. In this Section, we choose to focus on two characteristics: number counts and spectral

---

[8] We adopted the GMRT system parameters from *http://www.gmrt.ncra.tifr.res.in/gmrt_hpage/Users/doc /manual/UsersManual/node13.html*

Survey	Catalog flux	Perley-Taylor model flux	New model flux
74 MHz VLSS[a]	30.26 ± 3.08 Jy	34.67 Jy	30.26 Jy
151 MHz 6C[b]	26.31 Jy	31.25 Jy	29.81 Jy
151 MHz 7C[c]	26.53 Jy	”	”
159 MHz 3C[d]	30.0 ± 7.0 Jy	30.94 Jy	29.65 Jy
178 MHz 4C[e]	24.0 Jy	30.22 Jy	29.26 Jy
325 MHz WENSS[f]	27.12 ± 1.63 Jy	25.96 Jy	26.11 Jy

[a] Cohen et al. 2007

[b] Hales, Baldwin, & Warner 1988

[c] Hales et al. 2007 and references therein. Note that we use the peak flux rather than the integrated flux, as 3C 286 is unresolved on the 7C resolution.

[d] Edge et al. 1959; Bennett 1962

[e] Pilkington & Scott 1965; Gower, Scott & Wills 1967

[f] Rengelink et al. 1997. Note that we use the peak flux rather than the integrated flux, as 3C 286 is unresolved on the WENSS resolution.

Table 4: Flux measurements of 3C 286 from different radio survey catalogs at low frequency.

indices. When properly corrected for incompleteness, the number counts are an objective measure of the 150 MHz source population, that can be compared against models and other surveys. For individual sources, the spectral index can help to classify sources, but also to identify unusual sources like HzRGs.

4.1. Differential Source Counts

From the catalog we derived the Euclidean-normalised differential source counts. Because the source extraction criteria vary over the survey area, we used Figure 3 to correct for the missed fraction per flux bin. This will mainly affect the lowest two bins. Furthermore, the combined effect of random peaks in the background noise and a peak detection criteria causes a selection bias for positively enhanced weak sources (Eddington bias). In general, noise can scatter sources into other flux bins, most noticeably near the detection limit. Our attempts to correct for this effect though Monte-Carlo simulations were numerically unstable due to the low number counts in the lowest two bins. The effect on the higher bins was minimal, therefore we omit the Eddington bias corrections.

In Figure 6 the Euclidean normalized differential source counts are presented. Because no accurate source counts are available for 150 MHz at these low flux levels, we compare against the 330 MHz source count model from Wieringa (1991), scaled down to 150 MHz assuming various mean spectral indices. The correspondance between model and measurements is best for a mean spectral index of -0.8.

George & Stevens (2008) have determined Euclidean normalized differential source counts for 150 MHz GMRT observations on a field centered around ϵ Eridanus with a central background RMS value of 3.1 mJy beam^{-1}. They fit a single power-law slope of 0.72 to 113 sources over a flux range of 20 mJy–2 Jy, which is flatter than the value of 0.87 from our data over the range 40–400 mJy. The most likely explanation for this difference is the larger uncertainties on their lower source counts due to the higher background RMS and the smaller survey area that was used for analysis.

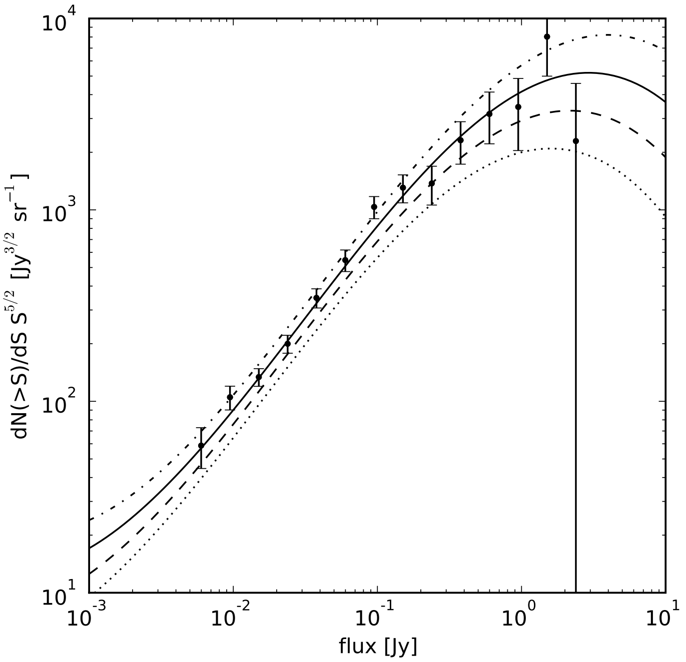

Figure 6: Euclidean-normalised differential source counts for the full 150 MHz catalog of ~ 600 sources, distributed over 15 logarithmic flux bins ranging from 3 mJy to 3 Jy (black dots plus poissonian error bars). Overplotted are models that were fitted to 325 MHz source counts from Wieringa (1991), scaled down in frequency to 150 MHz by assuming a constant spectral index for the whole source population. The spectral index values used are -0.0 (dotted line), -0.4 (dashed line), -0.8 (solid line) and -1.2 (dot-dash line).

The derived source counts agree well with a 151 MHz source count model by Jackson (2005) in which the FRii radio sources dominate the counts above ~ 50 mJy, while below the FRi sources are the most dominant population. The same model predicts a flattening in the power-law shape below ~ 10 mJy due to a growing fractional population of starburst galaxies. The flattening at low (sub-mJy) flux levels was first seen at 1.4 GHz (Windhorst 1985), and later also at frequencies below 1 GHz (e.g. at 610 MHz; Ibar et al. 2009). The true composition of this population of faint sources is still debated. Our survey depth is not sufficient to detect this flattening.

4.2. Spectral Indices

Because of the good match in resolution between the GMRT 150 MHz image and the deep WSRT 1.4 GHz image from De Vries et al. (2002), we can accurately determine spectral indices over a decade in frequency. Due to the high detection rate of 1.4 GHz sources at 150 MHz positions (Section 3.2), we do an automated search for 1.4 GHz counterparts within 25″ of the 150 MHz sources and ignore all sources for which we don't find counterparts. We find 417 matches, and therefore assume that the remaining 181 sources are either complex in morphology (with a large uncertainty in the centroid position) or outside the 1.4 GHz survey area. The spectral indices of matched sources are plotted in Figure 7. We find a median spectral index of -0.76, which is slightly lower than the median values of 0.79 (Cohen et al. 2004), 0.85 (Ishwara-Chandra & Marathe 2007) and 0.82 (Sirothia et al. 2009) found in similar high-resolution, low-frequency surveys. There is a steepening trend of the mean spectral index towards higher fluxes, indicating an increase of flat-spectrum sources in the source population towards lower flux levels. This effects is also seen between 1.4 GHz and 325 MHz (De Vries et al. 2002) and 1.4 GHz and 74 MHz (Cohen et al. 2004), but our measurement confirms this trend towards even lower flux levels.

From Figure 7 we highlight a group of 16 USS sources that have a spectral index below -1.3, which are candidate HzRGs (De Breuck et al. 2000). Table 5 lists these sources in decreasing flux order. Despite the relatively large uncertainty in 150 MHz flux for the faintest sources, the spectral index is still relatively well constrained due to the large frequency span. The angular distribution of the USS sources is quite peculiar (Figure 8). There are 6 sources that form 3 pairs within 6′ of eachother. These pairs, together with the remaining 10 single sources, appear to be randomly distributed across the FoV.

Croft et al. (2008) examine 4 candidate HzRGs, based on their low (≤ -0.87) spectral index between 1.4 GHz and 325 MHz. As, their candidate sources are also present in the 150 MHz catalog, we complement their data with our new spectral index measurements in Table 6. Both sources A and E appear to have fairly straight power-law spectra down to 150 MHz, while sources B and C appear to undergo considerable spectral flattening. Based on our selection criteria for USS sources, only source A would be considered a candidate HzRG.

4.3. Identification Fraction of Radio Sources versus Spectral Index

We investigate the spectral index-redshift correlation by determining the NIR K-band identification fraction of radio sources as function of spectral index. On average, steep spectrum sources are located at higher redshifts, therefore more difficult to detect. Using K-band has an advantage over (also available) shorter wavelength bands as this band suffers the least from extinction, and is known to correlate with redshift through the $K-z$ correlation (e.g., Willott et al. 2003).

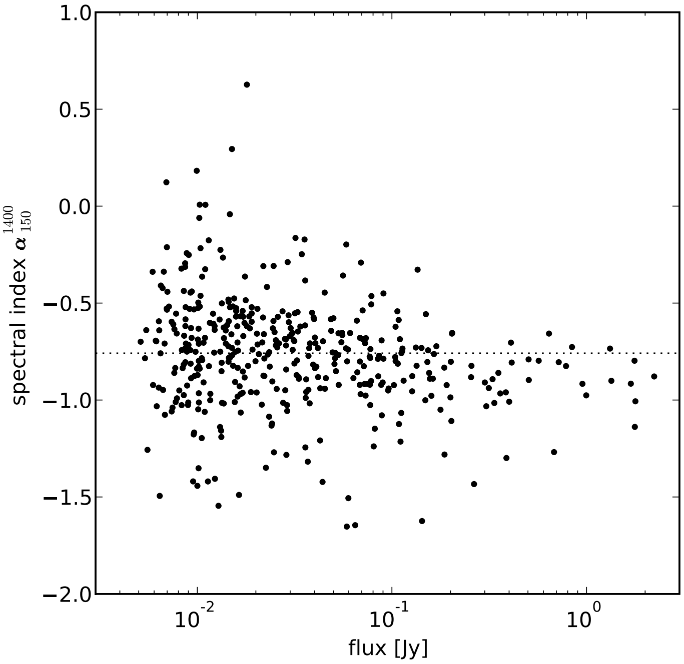

Figure 7: Spectral index for 417 sources between 1.4 GHz and 150 MHz. The detection limit is almost fully determined by the 150 MHz survey due to the sensitivity of the 1.4 GHz observations. The median spectral index is -0.76 (dotted line). 16 sources have a spectral index below -1.3.

We have identified possible optical counterparts of the radio sources using the the FLAMEX K_S-band catalogue (Elston et al. 2006). This survey covers 7.1 square degrees within the Boötes field. For the NIR identification we use the likelihood ratio technique described by Sutherland & Saunders (1992). This allows us to obtain an association probability for each NIR counterpart, taking into account the NIR magnitudes of the possible counterparts. Before, we removed all radio sources located outside the coverage area of the K_S-band images, or located within 20 pixels of the edge or other blanked pixels within individual K_S-band frames.

Following Sutherland & Saunders and Tasse et al. (2008), the probability that a NIR counterpart with magnitude m is the true NIR counterpart of the radio source is given by the likelihood ratio

$$\mathrm{LR}(r,m) = \frac{\theta(<m)\exp\left(-r^2/2\right)}{2\pi\,\sigma_\alpha\,\sigma_\delta\,\rho(<m)}, \tag{4}$$

with m the K_S-band magnitude of the NIR candidate, $\theta(<m)$ the a priori probability that the radio source has a NIR counterpart with a magnitude smaller than m, and $\rho(<m)$ the surface number density of NIR sources with a magnitude smaller than m. σ_δ^2 and σ_α^2 are the quadratic sums of the uncertainties in the radio and NIR positions in right ascension and declination, respectively. For the radio source positions and uncertainties we have taken the values from the 1.4 GHz WSRT catalogue, as the astrometric precision is better than the 150 MHz GMRT data. For

ID[a]	RA[b]	DEC[b]	150 MHz flux [mJy]	1.4 GHz flux [mJy]	α_{150}^{1400}
J142656+352230	$14^{\rm h}26^{\rm m}56.46^{\rm s}$	$35^\circ22'30.8''$	264.2 ± 26.6	11.31 ± 0.46	-1.43 ± 0.05
J143506+350059	$14^{\rm h}35^{\rm m}06.89^{\rm s}$	$35^\circ00'58.2''$	142.8 ± 14.5	4.02 ± 0.16	-1.62 ± 0.05
J143118+351549	$14^{\rm h}31^{\rm m}18.29^{\rm s}$	$35^\circ15'49.5''$	64.8 ± 6.9	1.74 ± 0.08	-1.65 ± 0.05
J143500+342531	$14^{\rm h}35^{\rm m}00.98^{\rm s}$	$34^\circ25'30.2''$	59.7 ± 6.2	2.18 ± 0.09	-1.51 ± 0.05
J143520+345950	$14^{\rm h}35^{\rm m}20.51^{\rm s}$	$34^\circ59'49.1''$	58.6 ± 6.2	1.55 ± 0.07	-1.65 ± 0.05
J143815+344428	$14^{\rm h}38^{\rm m}15.28^{\rm s}$	$34^\circ44'29.8''$	44.0 ± 4.8	1.93 ± 0.09	-1.42 ± 0.05
J143331+341012	$14^{\rm h}33^{\rm m}31.84^{\rm s}$	$34^\circ10'12.9''$	37.0 ± 4.1	2.04 ± 0.09	-1.32 ± 0.05
J142631+341557	$14^{\rm h}26^{\rm m}31.69^{\rm s}$	$34^\circ16'00.9''$	22.5 ± 3.6	1.16 ± 0.07	-1.35 ± 0.08
J142954+343516	$14^{\rm h}29^{\rm m}53.90^{\rm s}$	$34^\circ35'18.8''$	16.4 ± 2.4	0.62 ± 0.04	-1.49 ± 0.07
J142724+334714	$14^{\rm h}27^{\rm m}24.77^{\rm s}$	$33^\circ47'18.5''$	12.8 ± 2.8	0.43 ± 0.04	-1.55 ± 0.11
J143538+335347	$14^{\rm h}35^{\rm m}38.76^{\rm s}$	$33^\circ53'44.2''$	12.3 ± 2.2	0.56 ± 0.05	-1.41 ± 0.09
J143310+333131	$14^{\rm h}33^{\rm m}10.42^{\rm s}$	$33^\circ31'27.7''$	11.3 ± 2.2	0.50 ± 0.04	-1.42 ± 0.10
J143230+343449	$14^{\rm h}32^{\rm m}30.47^{\rm s}$	$34^\circ34'49.5''$	10.1 ± 1.8	0.52 ± 0.04	-1.35 ± 0.09
J142719+352326	$14^{\rm h}27^{\rm m}19.32^{\rm s}$	$35^\circ23'29.2''$	10.0 ± 3.4	0.42 ± 0.06	-1.44 ± 0.17
J143700+335920	$14^{\rm h}37^{\rm m}00.74^{\rm s}$	$33^\circ59'20.2''$	9.5 ± 2.5	0.42 ± 0.04	-1.42 ± 0.13
J143249+343915	$14^{\rm h}32^{\rm m}49.12^{\rm s}$	$34^\circ39'14.0''$	6.4 ± 1.8	0.24 ± 0.04	-1.49 ± 0.15

[a] From De Vries et al. (2002).
[b] Measured at 150 MHz.

Table 5: 150 MHz catalog selection of 16 USS sources with a spectral index below -1.3.

ID	RA[a]	DEC[a]	α_{325}^{1400} ([b])	α_{150}^{1400} ([c])
A	$14^{\rm h}26^{\rm m}31.75^{\rm s}$	$+34^\circ15'57.5''$	-1.48	-1.35 ± 0.08
B	$14^{\rm h}26^{\rm m}47.87^{\rm s}$	$+34^\circ58'51.0''$	-0.89	-0.56 ± 0.06
C	$14^{\rm h}27^{\rm m}41.84^{\rm s}$	$+34^\circ23'24.7''$	-0.98	-0.44 ± 0.13
E	$14^{\rm h}32^{\rm m}58.44^{\rm s}$	$+34^\circ20'55.4''$	-0.87	-0.95 ± 0.05

[a] As measured at 1.4 GHz; De Vries et al. (2002).
[b] Croft et al.
[c] This work.

Table 6: Spectral indices between 1.4 GHz and 150 MHz for four candidate HzRGs by Croft et al. (2008)

the FLAMEX survey we have used $0.3''$. The uncertainty-normalized angular distance is given by the parameter $r = \sqrt{(\Delta_\alpha/\sigma_\alpha)^2 + (\Delta_\delta/\sigma_\delta)^2}$, with Δ the positional difference in either α or δ between the possible NIR counterpart and radio source.

The probability $P(i)$ that candidate i is the true NIR counterpart is

$$P(i) = \frac{\mathrm{LR}_i(r,m)}{\sum_j \mathrm{LR}_j(r,m) + (1 - \theta(m_{\mathrm{lim}}))}, \tag{5}$$

with j running over all possible NIR counterparts. $\theta(m_{\mathrm{lim}})$ is the fraction of radio sources having a NIR counterpart at the magnitude limit of the NIR survey. The values for $\rho(< m)$ (surface number density of NIR sources) were estimated from the data itself using bins of 0.1 magnitude across the full survey area. The a-priori identification fraction $\theta(< m)$ was also estimated from the data itself, using the technique described by Ciliegi et al. (2003). This involves counting the surface number density of NIR sources around the radio sources as function of magnitude. This distribution is compared to a distribution of background objects, the overdensity of NIR sources around radio sources gives an estimate of $\theta(< m)$. We found $\theta(m_{\mathrm{lim}})$ to be 0.62.

We selected 368 radio sources that are present within both the 1.4 GHz and 150 MHz catalogs (matched within $6''$) and have a simple morphology (fitted with a single gaussian). We have computed the likelihood ratio of all NIR counterparts located within $20''$ from the radio position. We have defined a radio source to have a NIR counterpart if $\sum_j \mathrm{LR}_j(r,m) > 0.75$. The results are shown in Figure 9. The identification fraction is ~ 70 percent for $\alpha_{150}^{1400} < 0.7$, while for $\alpha_{150}^{1400} > 0.7$ the identification fraction drops to about 30 percent. This is in agreement with the spectral index-redshift correlation.

5. Conclusions and Future Plans

We have presented the results from a deep (central RMS < 0.7 mJy), high resolution ($26'' \times 22''$) radio survey at 150 MHz, covering the full NOAO Boötes field and beyond. This 11.3 square degree survey is among the deepest surveys at this frequency to date (e.g., Sirothia 2009). We produced a catalog of 598 sources detected at 5 times the local background RMS level, with source fluxes ranging from 3.9 Jy down to 5.1 mJy. We estimate our complenetess and contamination to be > 95 percent at 20 mJy and < 1 percent, respectively. The on-source dynamic range

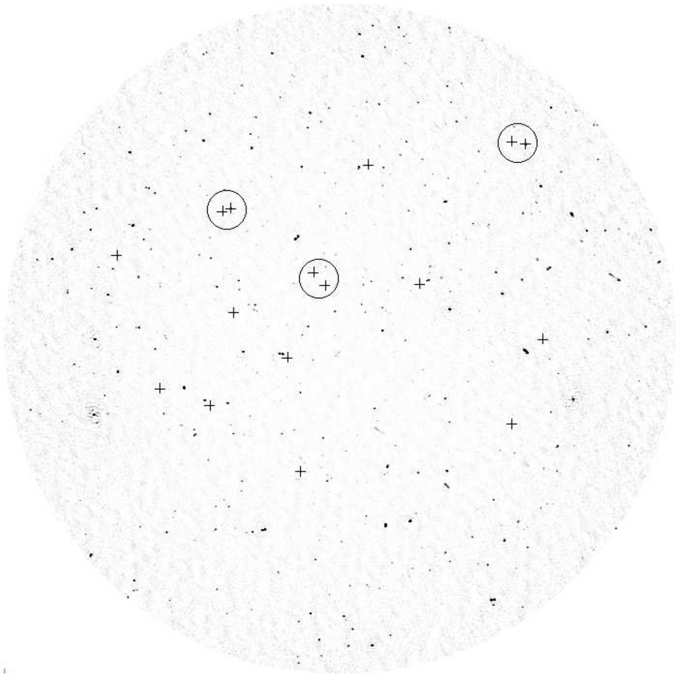

Figure 8: Greyscale map of the 150 MHz survey area with the positions of the 16 USS sources marked (plus signs). The angular distribution of USS sources is somewhat peculiar, as 6 sources have a neighbour within 6′ (marked by circles).

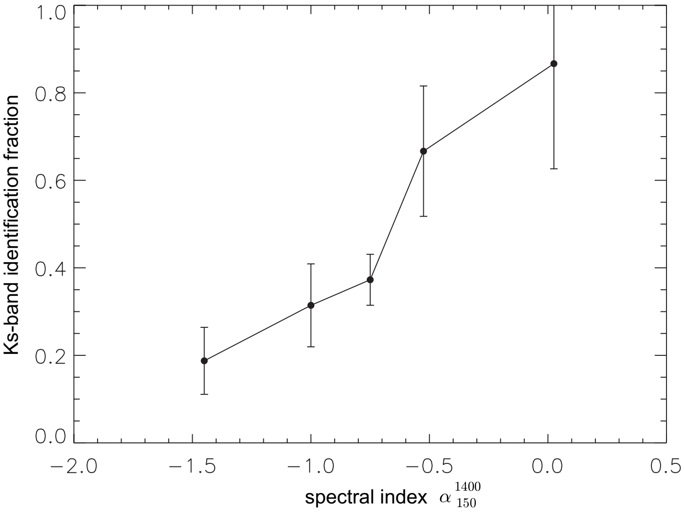

Figure 9: Identification fraction of radio sources in the near-infrared K_S-band as a function of spectral index between 1.4 GHz and 150 MHz.

is limited to $\sim$ 600, while off-source this rises to $>$ 4000. We expect that the significantly reduced sidelobe structure around bright sources due to direction-dependent phase calibration (SPAM; Intema et al. 2009) is now limited by direction-dependent amplitude errors.

The 150 MHz catalog allows for a detailed study of source populations in a relatively unexplored flux range. We have performed a brief analysis of the 150 MHz source catalog, focussed on determining source counts and spectral indices. From this analysis we draw the following conclusions: (i) The differential source counts are accurately determined over a flux range of 20 mJy up to 1 Jy. The counts are highly consistent with source counts at 325 MHz from Wieringa (1991), scaled to 150 MHz using a mean spectral index of -0.8. Using the same spectral index to extrapolate the results from 610 MHz and 1.4 GHz (e.g., Ibar et al. 2009), we expect a flattening of the differential source counts below $\sim$ 5 mJy at 150 MHz. Our survey is not sensitive enough to detect this flattening, which indicates a dominant population of FRI and FRII sources in our catalog (Jackson 2005).
(ii) The spectral indices of $>$ 400 sources between 150 MHz and 1.4 GHz have been accurately determined down to the lowest 150 MHz flux levels. The 1.4 GHz observations are more sensitive down to a spectral index of ~ -1.6, which are the steepest spectra that we find. We confirm the average flattening of source spectra towards lower flux levels. This can explain the slightly higher median spectral index of -0.76 as compared to other observations at 74 and 150 MHz, that lack either sensitivity at the low frequency end or the high frequency end.
(iii) We detect 16 out of 417 sources that have an USS with spectral index lower than -1.3, the lowest having a spectral index of -1.65. The fraction of USS sources is 3.8 percent, which is mostly dependent on the survey detection limit at 150 MHz. It is not straightforward to compare this fraction with other surveys that have different the detection limits at the high and/or low frequency end. Possibly the best match is a survey by Sirothia et al. (2009), that includes GMRT 150 MHz observations down to similar sensitivity. Using the same criteria, they find a USS fraction of 3.7 percent (14 out of 374), which is very consistent with our result.
(iv) A statistical analysis of the detection fraction of radio sources in K_S-band images, based on determining likelihood ratios, reproduces the expected correlation between spectral index and K_S-band detection. This links two other known correlation together, namely the $K - z$ correlation (e.g., Willott et al. 2003) and the correlation between spectral index and redshift (Tielens, Miley & Willis 1979; Blumenthal & Miley 1979).

We plan to continue our analysis of the 150 MHz source by matching against the wide variety of available catalogs at different spectral bands. A high priority task will be to study the properties of the 16 USS sources to determine if these objects are HzRGs, derive estimates of their redshifts and search the surrounding area for galaxies at similar redshift. This approach has been very succesful for the identification and study of galaxy cluster formation (e.g., Röttgering et al. 1994; Venemans et al. 2002; Intema et al. 2006).

The observations presented here are part of a larger survey with six additional, partly overlapping flanking fields observed with GMRT at the same frequency, covering a total survey area of $\sim$ 70 square degrees. Additionally, this same area is covered by extended WSRT observations using the 8 LFFE[9] bands between 115–165 MHz. We will combine these observations with the observations presented here to produce a combined high/low resolution catalog at $\sim$ 150 MHz to further facilitate the study of the low frequency sky, and in particular to facilitate the further search for USS radio sources.

---

[9] Low Frequency Front-End

Acknowledgements. The authors would like to thank the staff of the GMRT that made these observations possible. GMRT is run by the National Centre for Radio Astrophysics of the Tata Institute of Fundamental Research. This study made use of online available maps and catalogs from the WSRT Boötes Deep Field survey and the FLAMINGOS Extragalactic Survey. HTI acknowledges a grant from the Netherlands Research School for Astronomy (NOVA).

References

Athreya, R., 2009, ApJ, 696, 885
Becker, R.H., White, R.L. & Helfand, D.J., 1995, ApJ, 450, 559
Bennett, A.S., 1962, MmRAS, 68, 163
Bhatnagar, S., et al., 2008, A&A, 487, 419
Blumenthal, G., & Miley, G.K., 1979, A&A, 80, 13
Bridle, A.H. & Greisen, E.W., 1994, AIPS Memo 87
Briggs, D.S., 1995, PhD Thesis, New Mexico Institute of Mining Technology, Socorro, New Mexico, USA
Brown, M.J.I., et al., 2003, ApJ, 597, 225
Chandra, P., Ray, A. & Bhatnagar, S., 2004, ApJ, 612, 974
Ciliegi, P., et al., 2003, A&A, 398, 901
Cohen, A.S., et al., 2004, ApJS, 150, 417
Cohen, A.S., et al., 2007, ApJ, 134, 1245
Condon, J.J., et al., 1994, ASPC, 61, 155
Condon, J.J., 1997, PASP, 109, 166
Condon, J.J., et al., 1998, AJ, 115, 1693
Cool, R.J., et al., 2006, AJ, 132, 823
Cool, R.J., 2007, ApJS, 169, 21
Cornwell, T.J., and Perley, R.A., 1992, A&A, 261, 353
Cornwell, T.J., Braun, R. & Briggs, D.S, 1999, ASPC, 180, 151
Cotton, W.D., 1999, ASPC, 180, 357
Cotton, W.D., & Uson, J.M., 2008, A&A, 490, 455
Croft, S., et al., 2008, AJ, 135, 1793
De Breuck, C., et al., 2000, A&AS, 143, 303
De Breuck, C., et al., 2002, AJ, 123, 637
De Vries, W.H., et al., 2002, AJ, 123, 1784
Dey, A., et al., 1997, ApJ, 490, 698
Edge, D.O., 1959, MmRAS, 68, 37
Eisenhardt, P.R., et al. 2004, ApJS, 154, 48
Elston, R.J., et al., 2006, ApJ, 639, 816
George, S.J., & Stevens, I.R., 2008, MNRAS, 390, 741
George, S.J., & Ishwara-Chandra, C.H., 2009, arXiv:0903.2726, to appear in ASPC
Gower, J.F.R., Scott, P.F., & Wills, D., 1967, MmRAS, 71, 49
Hales, S.E.G., Baldwin, J.E. & Warner, P.J., 1988, MNRAS, 234, 919
Hales, S.E.G., et al., 2007, MNRAS, 382, 1639
Haslam, C.G.T., et al., 1982, A&AS, 47, 1
Houck, J.R., et al., 2005, ApJ, 622, 105
Ibar, E., et al., 2009, arxiv:0903.3600, submitted to MNRAS
Intema, H.T., et al., A&A, 456, 433
Intema, H.T., 2009, arxiv:0904.3975, accepted for publication in A&A
Ishwara-Chandra, C.H., & Marathe, R., 2007, ASPC, 380, 237
Jackson, C., 2005, PASA, 22, 36
Jacobson, A.M. & Erickson, W.C., 1992, Planet. Space Sci., 40, 447
Jannuzi, B.T., & Dey, A., 1999, ASPC, 191, 111
Jarvis, M.J., et al., 2001, MNRAS, 326, 1585
Kenter, A., et al., 2005, ApJS, 161, 9
Kettenis, M., et al., 2006, ASPC, 351, 497
Klamer, I.J., et al., 2006, MNRAS, 371, 852
McGreer, I.D., et al., 2006, ApJ, 652, 157
Miley, G.K., et al., 2006, ApJ, 650, 29
Miley, G.K., & De Breuck, C., 2008 A&A Rev., 15, 67
Murray, S.S., et al. 2005, ApJS, 161, 1
Nityananda, R., 2003, ASPC, 289, 29
Noordam, J.E., 2004, SPIE, 5489, 817
Perley, R.A., 1989, ASPC, 6, 259
Pilkington, J.D.H., & Scott, P.F., 1965, MmRAS, 69, 183
Rengelink, R.R., et al., 1997, A&AS, 124, 259
Reuland, M., et al., 2007, AJ, 133, 2607
Röttgering, H.J.A., et al., 1994, A&AS, 108, 79
Röttgering, H.J.A., et al., 1997, A&A, 326, 505
Röttgering, H.J.A., 2006, Astron. Nachr., 327, 118
Schwab, F.R., 1984, AJ, 89, 1076
Seymour, N., et al., 2007, ApJS, 171, 353
Sirothia, S.K., et al., 2009, MNRAS, 392, 1403
Sutherland, W., & Saunders, W., 1992, MNRAS, 259, 413
Tasse, C., 2007, A&A, 471, 1105
Tasse, C., 2008, A&A, 490, 879
Tielens, A.G.G.M., Miley, G.K., & Willis, A.G., 1979, A&AS, 35, 153
Thompson, A.R., 1999, PASP, 180, 11
Van Breugel, W., et al., 1999, ApJ, 518, 61
Venemans, B.P. et al., 2002, ApJ, 569, 11
Venemans, B.P., et al., 2007, A&A, 461, 823
Wieringa, M.H., 1991, PhD Thesis, Leiden University, Leiden, The Netherlands
Willott, C.J., et al., 2000, MNRAS, 316, 449
Windhorst, R.A., et al., 1985, ApJ, 289, 494
Willott, C.J., et al., 2003, MNRAS, 339, 173
Zirm, A.W., et al., 2008, ApJ, 680, 224